Tremella-like Ni$_3$S$_2$/MnS with ultrathin nanosheets and abundant oxygen vacancies directly used for high speed overall water splitting

Yong Zhang[a], Jiali Fu[a], Hui Zhao[a], Rijuan Jiang[a], Fang Tian[a], Renjie Zhang[a,b,c,*]

[a] Key Laboratory of Colloid and Interface Chemistry of the Ministry of Education of the P. R. China, Shandong University, Jinan 250100, P. R. China
[b] National Engineering Technology Research Center for Colloidal Materials, Shandong University, Jinan 250100, P. R. China
[c] Key Laboratory of Special Functional Aggregated Materials of the Ministry of Education of the P.R. China, Shandong University, Jinan 250100, P. R. China

ARTICLE INFO

ABSTRACT

The development of highly active and stable non-noble metal electrocatalysts for hydrogen evolution reaction (HER) and oxygen evolution reaction (OER) bifunctional performances is crucial for efficient water splitting. In this work, such electrocatalysts are obtained, first in two-step hydrothermal reactions to form Ni$_3$S$_2$/MnS nanosheets on Ni foam (NF/Ni$_3$S$_2$/MnS), then by slightly electroxidizing the Ni$_3$S$_2$/MnS to generate tremella-like Ni$_3$S$_2$/MnS-O with ultrathin nanosheets and abundant oxygen vacancies (denoted as NF/T(Ni$_3$S$_2$/MnS-O)) favorable for electrocatalyzing HER and OER. Benefiting from the abundant oxygen vacancies, tremella-like ultrathin nanosheets with hierarchical porous structure and large active surface area, NF/T(Ni$_3$S$_2$/MnS-O) shows high catalytic performance, including lower overpotential and electrochemistry stability for both HER and OER than so far reported MnO$_x$ and other metal oxides/sulfides. The NF/T(Ni$_3$S$_2$/MnS-O) directly used as bifunctional electrodes for overall water splitting exhibits a low voltage of 1.54 V with a low overpotential of 0.31 V at a current density of 10 mA cm^{-2}, a fast H$_2$ and O$_2$ evolution speed of 4.13 and 2.04 μmol min^{-1} and a good electrochemistry stability with unchanged current density of 10 mA cm^{-2} for 50 h.

1. Introduction

The contradictory issues between rapidly growing global energy demands and limited fossil fuels should be urgently dissolved by pursuing clean and sustainable energy alternatives [1]. Hydrogen gas as an alternative can be obtained by electrochemical water splitting [2–5]. Commercial catalysts for cathodic hydrogen evolution reaction (HER) and anodic oxygen evolution reaction (OER) are mainly Pt/C and IrO$_2$/RuO$_2$ based on noble metals [2]. However, their large-scale application is limited by high cost and low abundance in the earth [6,7]. Therefore, it is highly desirable to develop efficient low-cost electrocatalysts based on earth-abundant elements for water splitting to replace such noble metal electrocatalysts. Manganese dioxide (MnO$_2$) nanosheets on nickel foam (NF) for catalyzing HER and OER were recently reported [8]. Good electrical conductivity is essential for electrocatalyst [9,10]. Manganese sulfide (MnS) with narrower band gap (E_g) (3.0) than that of MnO$_2$ (3.6) should exhibit larger conductivity. The oxygen reduction reaction of MnS has also been studied, however its OER and HER have not been reported. Moreover, besides simply studying HER and OER, overall water splitting should be studied to reduce the economic costs and simplify the water electrolyzing system.

Heterostructured nanomaterials has been widely reported for electrocatalysis [11], photocatalysis [12–14] and supercapacitor [15], due to their unique heterostructure optimizing electronic structure, so that they show better performance than single component [16]. Metal sulfides as electrocatalysts, to further improve electrocatalytic performance, can be slightly electrooxidized to metal oxides/hydroxides with abundant oxygen vacancies (OVs) under high voltage in alkaline media [17]. The obtained heterostructure display better electrocatalytic performance than those before oxidation [17,18]. The reason may be that there are synergistic electronic interactions between the different components that make the compounds better than the simple oxides, due to OVs improving conductivity [19,20], facilitate the kinetic processes of the adsorption of H$_2$O for HER [21] or OH$^-$ for OER [22], the evolution and desorption of H$_2$ or O$_2$ [23,24]. Moreover, the derived metal oxides/hydroxides could be formed as high active surface area and hierarchical porous structure that assure sufficient exposure of OVs [25] and facilitates the mass transfer of H$_2$O for HER or OH$^-$ for OER to and H$_2$ or O$_2$ from the active surface [26], synergistically speeding up HER or OER.

Last but not least, most electrocatalysts were not used directly but mixed with compounds including polymer binders and carbon materials followed by coating on electrodes [27–29]. Such processes cannot guarantee the electrocatalytic activity due to possible damage of original microstrucures or loss of active surfaces. An efficient solution is to assemble active materials on current collector and use them directly as electrodes.

In this work, we obtain tremella-like Ni_3S_2/MnS with ultrathin nanosheets and abundant OVs on NF (denoted as NF/T(Ni_3S_2/MnS-O)) by hydrothermal synthesis and slight electrooxidation. The NF/T(Ni_3S_2/MnS-O) with hierarchical pores and large active surface area, directly used as electrodes for water splitting yields better HER and OER bifunctional performances including efficient electrocatalytic activities and higher stability than so far reported MnO_x and other metal oxides/sulfides.

2. Experimental section

2.1. Fabrication of NF/MnO_2

Firstly, NF was ultrasonically washed with acetone, and then with HCl (1.0 M) for 10 min to remove the oxide layer on the NF surface, and then washed with pure water and ethanol for several times, followed by drying at 60 °C for 4 h. NF/MnO_2 was synthesized using a simple hydrothermal method, where the composition was referred to literature [8]. A piece of cleaned NF (1 cm × 3 cm) was put into a Teflon-lined autoclave (50 mL) containing 40 mL of 25 mM $KMnO_4$. Then the autoclave was maintained at 180 °C for 1 h. The obtained NF/MnO_2 was rinsed by pure water for three times followed by rinsing with ethanol for one time, and finally dried at 60 °C for 4 h.

2.2. Preparation of NF/Ni_3S_2/MnS

$Na_2S·9H_2O$ (7.23 g) was dissolved in H_2O (30 mL) at room temperature under stirring. The Na_2S solution was transferred into a Teflon-lined autoclave (50 mL), and then the NF/MnO_2 was put into the autoclave. The autoclave was maintained at 160 °C for 8 h. After cooling down to room temperature, the obtained NF/Ni_3S_2/MnS was washed with pure water for three time followed by rinsing with ethanol for one time, and finally dried at 60 °C for 6 h.

2.3. Preparation of NF/T(Ni_3S_2/MnS-O)

The NF/T(Ni_3S_2/MnS-O) was prepared through replacing the surfacial sulfide of NF/Ni_3S_2/MnS with oxides containing OVs by a continuous electrooxidation at 1.6 V *versus* reversible hydrogen electrode (*vs.* RHE) for 8 h in 1.0 M KOH [18].

2.4. Characterization

The morphology and microstructure of the above samples were observed by scanning electron microscopy (SEM) (Zeiss Gemini300, Germany) and TEM (JEOL JEM-1011, Japan). The SEM species were prepared by cutting the samples using a scissor, and then sputtered with gold. The elemental mapping was obtained from high resolution energy dispersive X-ray spectrometer (EDS, Bruker, Germany) attached to SEM. The investigation depth of X-ray is *ca.* 5 μm. High resolution TEM (HRTEM) images and selected area electron diffraction (SAED) were obtained on a TEM instrument (JEOL JEOL-2100 F, Japan) with an acceleration voltage of 200 kV. T(Ni_3S_2/MnS-O) for TEM and HRTEM measurement was cut from NF by a knife and dispersed in water, and then 5 μL of suspensions were dropped on copper grids followed by air drying. X-ray diffraction (XRD) patterns were collected through a D8 Advance X-ray diffractometer (Bruker, Germany) operated at 40 mA and 40 kV with the Cu (Kα) radiation (λ = 1.54184 Å) in an angular range (2θ) of 10–70° at an interval of 0.04° and a scanning rate of 1°

min^{-1}. X-ray photoelectron spectroscopy (XPS) was taken on a 250Xi spectrometer system (Thermo Scientific, USA) with the Al (Kα) radiation (X-ray energy 1486.6 eV) with an energy analyzer working in the pass energy mode at 100.0 eV. The binding energy was calibrated against the C1s line and the investigation depth is *ca.* 5 nm. Nitrogen (N_2) adsorption-desorption isotherms were recorded with an ASAP 2020 HD88 instrument (Micromeritics, USA). The BET species were prepared by cut into pieces using a scissor. The specific surface area of NF/T(Ni_3S_2/MnS-O) and NF/Ni_3S_2/MnS were obtained by calculating the adsorption branch with the BET method. Electron spin resonance (ESR) spectra were obtained with the JEOL JESX320 at a frequency of 9.184 GHz at room temperature. UV–vis diffuse reflectance spectra (DRS) were measured using a Cary 5000 spectrophotometer fitted with an integrating sphere attachment from 200 to 800 nm.

2.5. Electrochemical measurement

The electrocatalytic activities were carried out using a CHI760E electrochemical workstation with a three-electrode cell, where Ag/AgCl (sat. KCl) and graphite rod were used as the reference and counter electrodes, respectively. All our own samples (1 cm × 1 cm) were directly used as the working electrodes. For NF/Pt/C or NF/IrO_2 as comparison, 20 mg of 20% Pt/C or IrO_2 was dispersed in a mixture of ethanol (985 μL) and Nafion solution (15 μL), respectively, followed by ultrasonic treatment to obtain a homogenous ink. Then, 100 μL of ink was loaded onto a piece of NF (1 cm × 1 cm) by drop-coating with a loading mass of 2.0 mg cm^{-2}. The mass loading of T(Ni_3S_2/MnS-O) is 1.8 mg cm^{-2}. N_2 saturated 1.0 M KOH electrolyte was used during electrochemical tests. All potential values (*vs.* RHE) were calculated by the equation: E (*vs.* RHE) = E (*vs.* Ag/AgCl) + 1.0374 V. Linear sweep voltammetry (LSV) curves were collected at a scan rate of 5 mV s^{-1} with 90% *iR* compensation. Chronopotentiometric tests were recorded to explore the stability of the samples at current density of 10 mA cm^{-2}. The area for calculating current density is the actual area of NF. Cyclic voltammetry (CV) tests were carried out with various scan rates ranging from 5 to 50 mV s^{-1} to estimate the electrochemical active surface area (ECSA). The ECSA was calculated by the following Eq. (1):

$$ECSA = \frac{C_{dl}}{C_s} \times s \tag{1}$$

where the C_{dl} is the double layer capacitance gained by the CVs test; the C_s is an average value with a general specific capacitance of 0.04 m F cm^{-2} in 1.0 M KOH, s is the geometric area of the working electrode.) [4].

The amount of H_2 evolved from the work electrodes at a potential of -0.5 V (*vs.* RHE) for HER was directly measured using the GC-7900 gas chromatography (Techcomp, China). The amount of O_2 evolved from the work electrodes at the potential of 1.65 V (*vs.* RHE) for OER was measured by gas chromatography.

The theoretical amount of H_2 evolved during overall water splitting was calculated by the following Eq. (2):

$$n(H_2) = \frac{It}{2F} \tag{2}$$

where n is the amount of H_2 gas (mol), *I* is the measured current (A), *t* is the water splitting time (s) and *F* is the Faraday constant (96485 C mol^{-1}).

The theoretical amount of O_2 evolved during overall water splitting was calculated by the following Eq. (3):

$$n(O_2) = \frac{It}{4F} \tag{3}$$

where n is the amount of O_2 gas (mol), *I* is the measured current (A), *t* is the water splitting time (s) and *F* is the Faraday constant (96485 C mol^{-1}).

The active surface site density and per-site turnover frequency

(TOF) for the catalyst is calculated using the relative roughness factor (RF) of the catalysts calculated by the following Eq. (4) [30]:

$$RF = \frac{C_{dl}}{C_s} \qquad (4)$$

where the C_{dl} is the double layer capacitance gained by the CVs test, Cs is an average value with a general specific capacitance of 0.04 m F cm^{-2} in 1.0 M KOH, which gives the number (n_s) of surface active sites of 1.761×10^{15} [31].

The number (N) of surface active sites per cm^{-2} is calculated based on the following Eq. (5):

$$N = RF \times n_s \qquad (5)$$

The TOF for OER is calculated by the following Eq. (6):

$$TOF = \frac{j \times N_A}{4 \times 10^3 NF} \qquad (6)$$

where j is the measured current density for OER, N_A is Avogadro constant (6.022×10^{23}), F is the Faraday constant (96485 C mol^{-1}).

The electrochemical impedance analysis was obtained by electrochemical impedance spectroscopy (EIS) using an impedance analyzer (Zahner IM6, Germany). The measurement was carried out in the frequency range of $0.1-10^5$ Hz with voltage amplitude of 5 mV.

3. Result and discussion

The formation process for the NF/T(Ni$_3$S$_2$/MnS-O) catalyst is illustrated in Fig. 1. On the surface of NF (Fig. 1a), MnO$_2$ nanosheets were first grown by a hydrothermal method in the presence of KMnO$_4$ (denoted as NF/MnO$_2$, Fig. 1b). The NF might be oxidized under the hydrothermal reaction. However, it is not detected by XRD to be shown later, so it can be ignored due to very low content. Subsequently, MnO$_2$ on NF was converted to MnS in Na$_2$S solution, along with the Ni$_3$S$_2$ formed due to partial vulcanized Ni in NF (Fig. 1c). Finally, Ni$_3$S$_2$/MnS on NF was electrooxidized to form NF/T(Ni$_3$S$_2$/MnS-O) in KOH solution (Fig. 1d).

The product morphologies after each step in Scheme 1 are observed by TEM and SEM. The morphology of NF/MnO$_2$, NF/Ni$_3$S$_2$/MnS and NF/T(Ni$_3$S$_2$/MnS-O) are similar, all showing closely connected tremella-like ultrathin nanosheets of $ca.$ 2 nm thick (Figs. 2 and 3). The T(Ni$_3$S$_2$/MnS-O) layer on NF is $ca.$ 1.5 μm thick (Fig. S1) with homogeneously distributed Ni, Mn, S and O elements (Fig. S2), where the O element is introduced during electrooxidation. Magnified observation reveals that the O element exist in a nanolayer of amorphous metal oxides of 3-4 nm thick on the topmost edge of each T(Ni$_3$S$_2$/MnS-O) nanosheet (Fig. 3e). In the HRTEM image of NF/T(Ni$_3$S$_2$/MnS-O), there are fringes with the spacing of 0.26 and 0.17 nm, corresponding to the (200) lattice of MnS and (122) lattice of Ni$_3$S$_2$, respectively, similar to those for NF/Ni$_3$S$_2$/MnS before electrooxidation (Fig. 2e and f).

The sequential changes from NF/MnO$_2$ to NF/Ni$_3$S$_2$/MnS and to NF/T(Ni$_3$S$_2$/MnS-O) are confirmed by XRD and Raman spectroscopy.

The XRD peak of NF/T(Ni$_3$S$_2$/MnS-O) reveals that the composite is composed of MnS (JCPDS No. 65-0891) and Ni$_3$S$_2$ (JCPDS No. 44-1418), entirely different from that of NF/MnO$_2$ (JCPDS No. 86-0666) (Fig. 4). The XRD peaks at 34.3° and 55.2° (2θ) correspond to the (200) lattice of MnS and (122) lattice of Ni$_3$S$_2$, respectively. The changed intensity rate of relatively less intense and broaden XRD peaks of the NF/T(Ni$_3$S$_2$/MnS-O) corresponding to different crystal faces may be due to the formation of amorphous metal oxides nanolayer [32]. Moreover, the XRD peaks of Ni$_3$S$_2$ and MnS in NF/T(Ni$_3$S$_2$/MnS-O) shift to higher angles, which might result from the shrinkage of lattices when S^{2-} ions (ion radius of ~1.84 Å) are partially substituted by O^{2-} ions (ion radius of ~1.4 Å) with a smaller radius. Two intense peaks at 45° and 52° originate from the NF substrate [33]. The two peaks in the Raman spectra of NF/T(Ni$_3$S$_2$/MnS-O) at 351.1 and 635 cm^{-1}, corresponding to the stretching vibrations of Ni$_3$S$_2$ [34] and MnS [35], respectively, are slightly changed after electrooxidation (Fig. S4).

Electrooxidation generates OVs in the amorphous metal oxides layer on surface of NF/T(Ni$_3$S$_2$/MnS-O), as confirmed by XPS and electron spin resonance (ESR). The O 1s peak at 531.6 eV in XPS (Fig. 5b), which can be divided into three peaks. The O$_L$ peak at 529.3 eV is assigned to the O in the metal −O bond. The O$_V$ peak of oxygen deficient regions [36] within the lattice is located at 531.2 eV. The O$_C$ peak at 532.5 eV is associated with the O in the hydroxy species of adsorbed water molecules [18]. The percentage of O$_L$, O$_V$ and O$_C$ are 14.3, 61.7 and 24 at%, respectively, suggesting that relatively abundant OVs appeared in amorphous metal oxides layer on the surface of NF/T(Ni$_3$S$_2$/MnS-O) are generated during electrooxidation. As comparison, the O 1s spectrum for NF/Ni$_3$S$_2$/MnS shows two peaks of O$_L$ and O$_C$, which are associated with the O in the metal–O bond and the O in adsorbed water molecules from air, respectively. The reason of the metal-O bond generated in NF/Ni$_3$S$_2$/MnS is the slight oxidation of metal sulfides in air. OVs should be generated in amorphous metal oxides layer on the surface of NF/T(Ni$_3$S$_2$/MnS, when the lattice oxygen atoms of metal oxides (electrooxidized from the sulfides) are further oxidized to form desorbed O$_2$ in electrooxidation, as also observed by Guo and co-authors for NiS$_2$/CoS$_2$ [18]. Furthermore, the NF/T(Ni$_3$S$_2$/MnS-O) exhibits a strongly symmetrical ESR signal at g = 2.003 than that of NF/Ni$_3$S$_2$/MnS (Fig. 5c), which also demonstrates the existence of OVs in the amorphous metal oxides layer on the surface of NF/Ni$_3$S$_2$/MnS after electrooxidation [37]. In addition, OVs narrow down the band gap (E_g) of NF/T(Ni$_3$S$_2$/MnS-O), as confirmed by UV–vis diffuse reflectance spectra (DRS) (Fig. 5d and e). The absorption band of NF/T(Ni$_3$S$_2$/MnS-O) is slightly red-shifted, suggesting that NF/T(Ni$_3$S$_2$/MnS-O) displays a narrower E_g [38]. The E_g of NF/T(Ni$_3$S$_2$/MnS-O) is calculated using the following Eq. (7) [39]:

$$\alpha h\nu = A(h\nu - E_g)^2 \qquad (7)$$

where α, h, ν, A and E_g denote the absorption coefficient, Planck constant, light frequency, a constant and band gap, respectively. The plots of $(\alpha h\nu)^{1/2}$ against photon energy are shown in Fig. 5e. The calculated
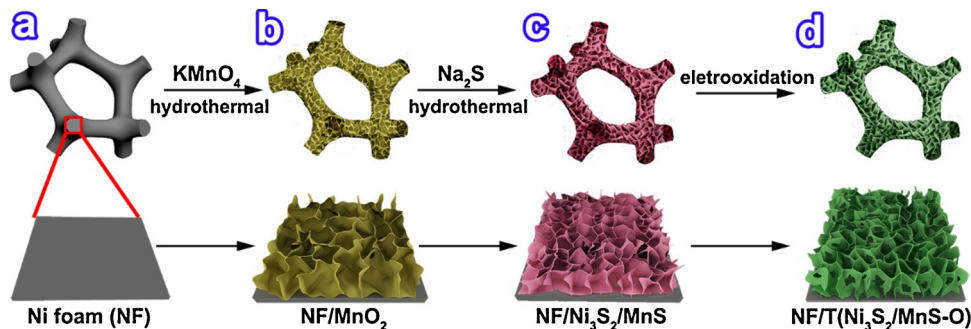

Fig. 1. Schematic of the formation of NF/T(Ni$_3$S$_2$/MnS-O) on NF. Only a side of NF is illustrated, and one layer of NF/MnO$_2$, NF/Ni$_3$S$_2$/MnS, and NF/T(Ni$_3$S$_2$/MnS-O) are illustrated to make the morphologies of MnO$_2$, Ni$_3$S$_2$/MnS and T(Ni$_3$S$_2$/MnS-O) nanosheets legible.
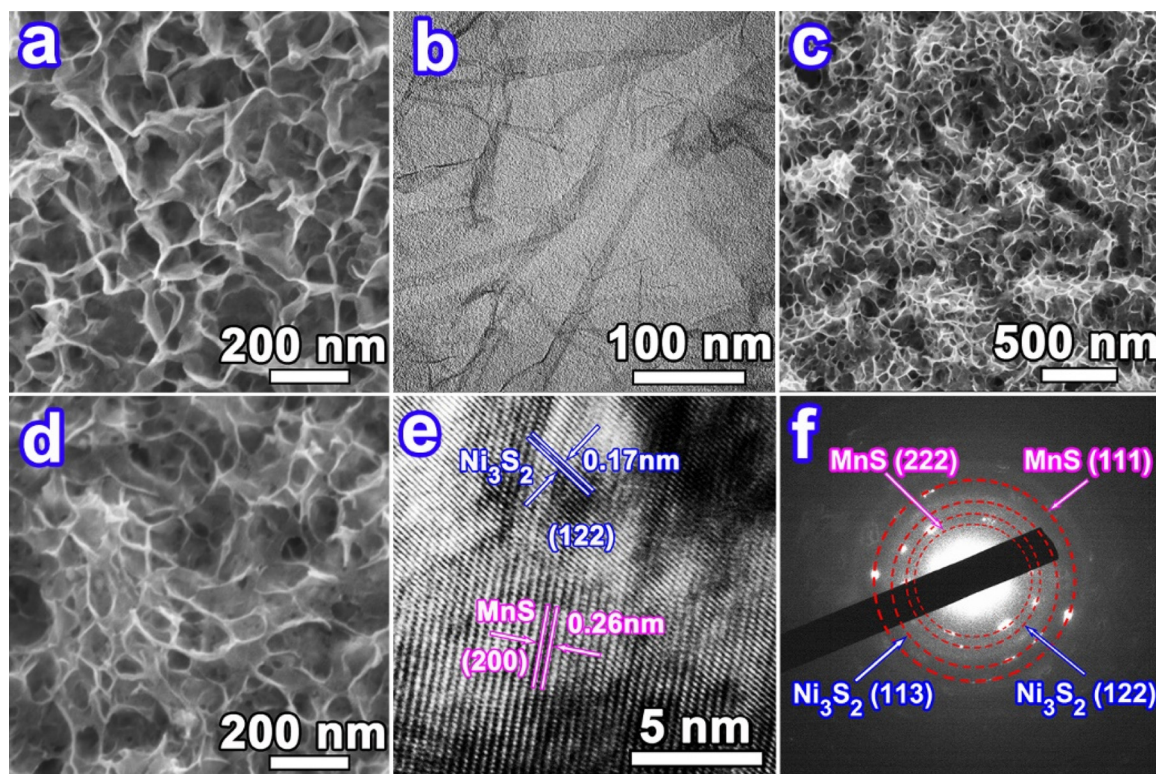
Fig. 2. (a) SEM image and (b) TEM image of NF/MnO₂. (c and d) SEM images, (e) HRTEM image and (f) SAED image of NF/Ni₃S₂/MnS nanosheets.

E_g of NF/T(Ni₃S₂/MnS-O) is 2.86 eV, lower than those of NF/MnO₂ (4.06 eV), NF/Ni₃S₂ (3.62 eV) and NF/(Ni₃S₂/MnS) (2.98 eV). Combining O 1s XPS, ESR with UV–vis DRS, we can draw a conclusion that the OVs are successfully introduced and responsible for the narrowed band gap of NF/T(Ni₃S₂/MnS-O). OVs are of great importance since

they improve conductivity [19,20], facilitate the kinetic processes of the adsorption of H₂O for HER [21] or OH⁻ for OER [22], the evolution and desorption of H₂ or O₂ from the electrocatalyst surface.

The Ni 2p, Mn 2p and Mn 3 s spectra further confirm the OVs generated in the electrooxidation process. The Ni 2p spectrum of NF/
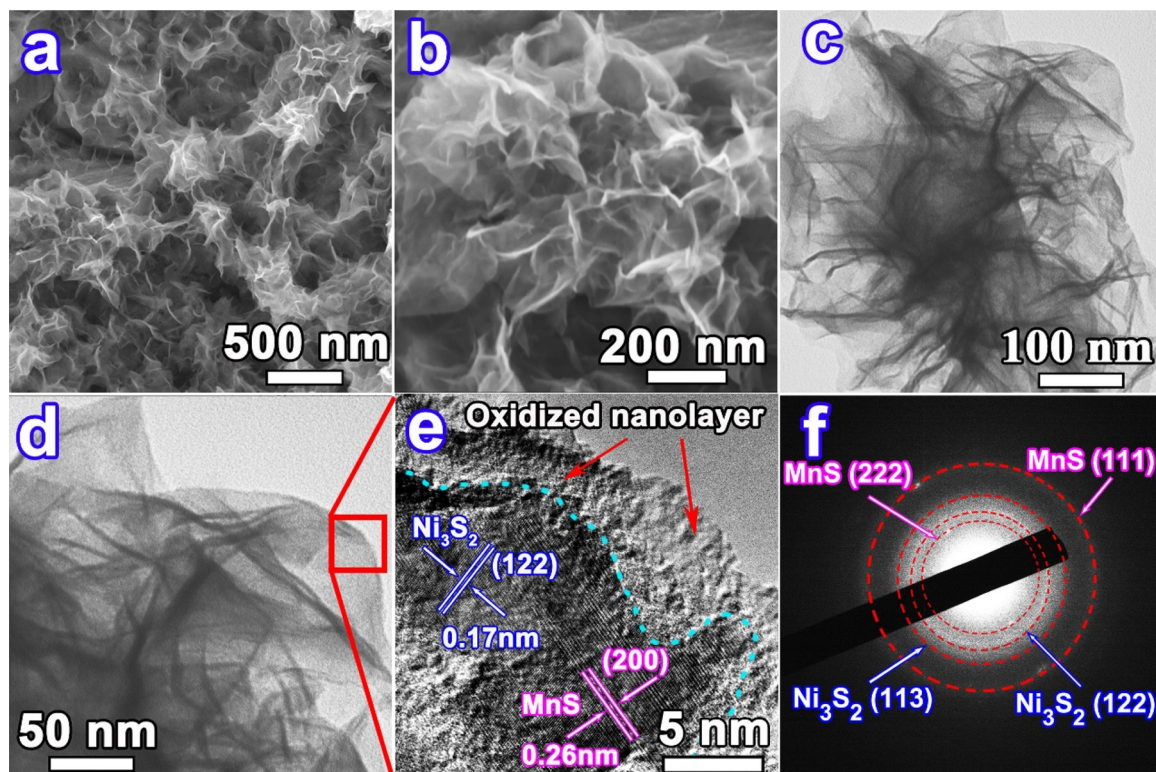

Fig. 3. (a and b) SEM images, (c and d) TEM images, (e) HRTEM image and (f) SAED image of NF/T(Ni₃S₂/MnS-O) nanosheets.
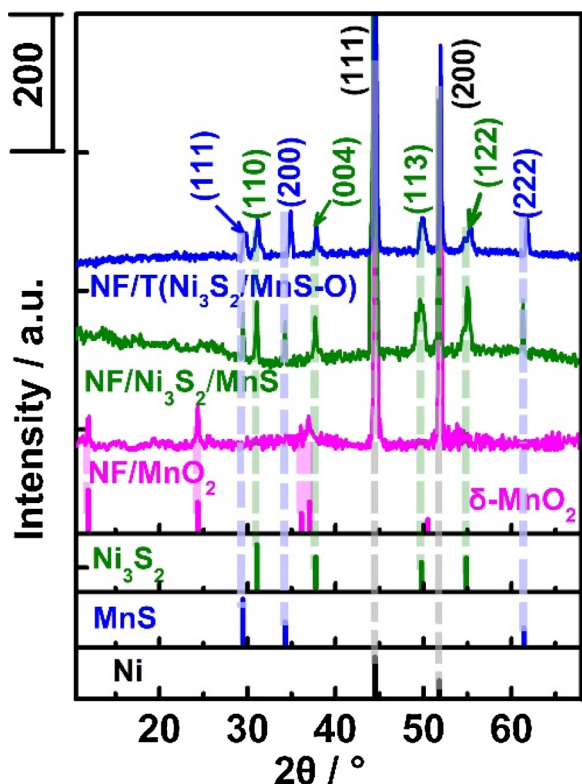
Fig. 4. XRD patterns of NF/T(Ni₃S₂/MnS-O), NF/Ni₃S₂/MnS, NF/MnO₂, Ni (JCPDS No.04-0850), δ-MnO₂ (JCPDS No. 86-0666), MnS (JCPDS No. 65-0891), Ni₃S₂ (JCPDS No. 44-1418) and MnS (JCPDS No. 65-0891).

T(Ni₃S₂/MnS-O) exhibits two spin–orbit doublets characteristic of Ni $2p_{1/2}$ and Ni $2p_{3/2}$ peaks centered at 872.8 and 855.5 eV, respectively, as well as corresponding shakeup satellites (identified as "Sat.") (Fig. 5f) [34]. The Ni $2p_{3/2}$ peak at 855.5 eV can be deconvoluted into three peaks at 852.2, 855.4 and 856.9 eV, corresponding to Ni$^{\delta+}$ (δ is close to 0), Ni^{2+} and Ni^{3+} species, respectively. Based on the integration of corresponding peaks, the ratio of Ni^{3+}/Ni^{2+} (46.6 at%) in NF/T(Ni₃S₂/MnS-O) is much larger than that of NF/Ni₃S₂/MnS (27.6 at%), indicating the Ni₃S₂ on the surface is also oxidized [40]. Similarly, the Mn $2p_{3/2}$ peak of NF/T(Ni₃S₂/MnS-O) shifts to 641.7 eV, 0.8 eV larger than that of NF/Ni₃S₂/MnS (640.9 eV) (Fig. 5g), implying that S atoms are replaced by the O atoms, which increase the binding energy of surrounding Mn atoms [9]. The Mn $2p_{3/2}$ peak of NF/T(Ni₃S₂/MnS-O) can be deconvoluted into three peaks at 641.7, 642.3 and 644.4 eV, corresponding to Mn^{2+}, Mn^{3+} and Mn^{4+} species, respectively, different from that of NF/Ni₃S₂/MnS before electrooxidation. Furthermore, the energy separation ΔE(Mn 3 s) value of NF/T(Ni₃S₂/MnS-O) is 5.16 eV, lower than that of NF/Ni₃S₂/MnS (5.77 eV) (Fig. 5h), demonstrating the Mn in NF/T(Ni₃S₂/MnS-O) exhibits a higher valance, based on the ΔE(Mn 3 s) of 5.9 eV for Mn^{2+}, 5.4 eV for Mn^{3+} and 4.5 eV for Mn^{4+} [41], respectively. The binding energies and species of Ni 2p, Mn 2p and Mn 3 s confirm the enhanced eletrooxidation to obtian NF/T(Ni₃S₂/MnS-O). In addition, the comparison of S 2p spectra between NF/Ni₃S₂/MnS and NF/T(Ni₃S₂/MnS-O) indicates that the sulfide on the surface disappears after the electrooxidation (Fig. 5i) [18]. The result also demonstrates that the amorphous metal oxides layer appears on surface of NF/T(Ni₃S₂/MnS-O). The thickness is consistent with the topmost amorphous electrooxidized layer of 3–4 nm as observed by HRTEM. It should be noted that the sulfide on the surface is not detected, although the investigation depth of XPS is ca. 5 nm, due to the low relative sensitivity factor of S species.
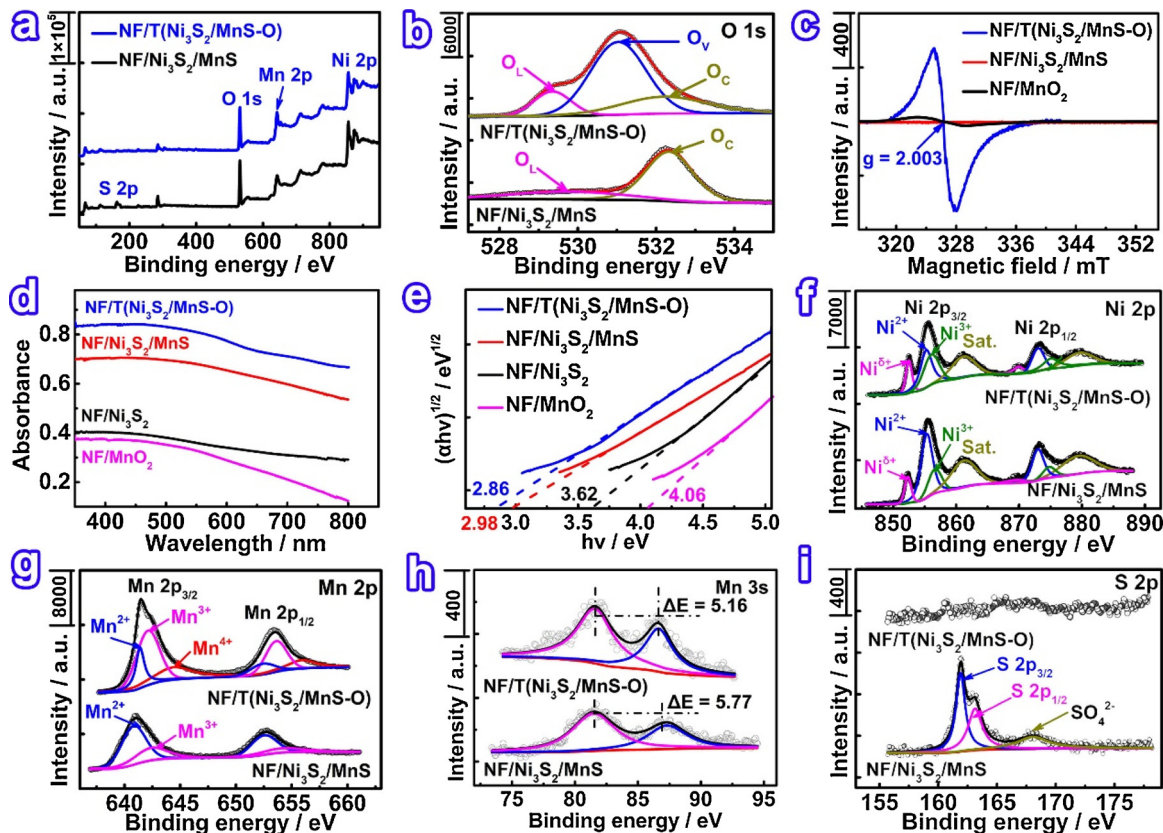

Fig. 5. (a and b) Survey XPS and O 1s XPS spectra of NF/Ni₃S₂/MnS and NF/T(Ni₃S₂/MnS-O). (c) ESR spectra of NF/MnO₂, NF/Ni₃S₂/MnS and NF/T(Ni₃S₂/MnS-O). (d) UV–vis DRS and (e) Plots of $(\alpha h\nu)^{1/2}$ against photon energy of NF/MnO₂, NF/Ni₃S₂, NF/Ni₃S₂/MnS and NF/T(Ni₃S₂/MnS-O). (f–i) Ni 2p, Mn 2p, Mn 3 s and S 2p XPS spectra of NF/Ni₃S₂/MnS and NF/T(Ni₃S₂/MnS-O).
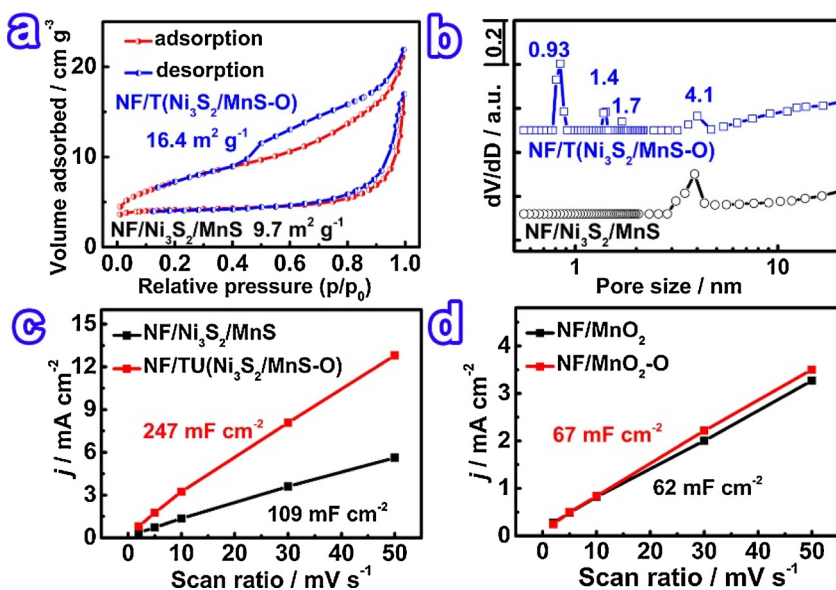
NF/T(Ni_3S_2/MnS-O) exhibits the hierarchical porous structure (Fig. 6a and b). The specific surface area and pore volume of NF/T(Ni_3S_2/MnS-O) (16.4 $m^2 g^{-1}$ and 0.037 $cm^3 g^{-1}$) are larger than those of NF/Ni_3S_2/MnS (9.7 $m^2 g^{-1}$ and 0.011 $cm^3 g^{-1}$). The values of BET and pore volume are low due to low mass loading of catalysts and the electrooxidation of NF. However, the obvious hysteresis loop at a relative pressure from 0.4 to 0.9 indicates the existence of mesopores mainly from the NF and between nanosheets in NF/T(Ni_3S_2/MnS-O) (Fig. 6a). Especially, the relatively steep increase in the nitrogen uptake at a low relative pressure ($p/p_0 < 0.1$) indicates the existence of micropores formed during the electrooxidation in NF/T(Ni_3S_2/MnS-O), entirely different from that of NF/Ni_3S_2/MnS, indicating a higher porous structure, as also observed by Cui and coworkers for CoS_2 [25]. The ratio of micropores, mesopores and macropores to all pores is calculated to be 2.5, 16.6 and 80.9%, respectively. The hierarchical porous structure ensures sufficient exposure of OVs and facilitates the mass transfer of H_2O for HER or OH- for OER to and H_2 or O_2 from NF/T(Ni_3S_2/MnS-O), synergistically speeding up HER or OER [26], consequently implying potential high electrochemical performance to be confirmed latter for NF/T(Ni_3S_2/MnS-O).

The areal capacitance of NF/T(Ni_3S_2/MnS-O) also increases after the electrooxidation as evaluated by the electrochemical double layer capacitance, which is used to estimate the magnitude of electrochemical active surface area (ECSA) [4,25]. The NF/T(Ni_3S_2/MnS-O) has an increased CV area with the enhanced areal capacitance of 247 $mF cm^{-2}$ and corresponding ECSA of 1543 cm^2 (Figs. 6c, S6), which is about 2 times of that of NF/Ni_3S_2/MnS (109 $mF cm^{-2}$ and 681 cm^2) and 4 times of that of the NF/MnO_2 (62 $mF cm^{-2}$ and 418 cm^2) (Fig. 6d). Accordingly, the NF/T(Ni_3S_2/MnS-O) should be more electrochemically active than NF/Ni_3S_2/MnS and NF/MnO_2.

Abundant OVs, together with hierarchical porous structure and large surface active area enable NF/T(Ni_3S_2/MnS-O) to show excellent HER performance (Movie S1). NF/T(Ni_3S_2/MnS-O) requires a low overpotential of 116 mV to deliver the current density of $-10 mA cm^{-2}$ (Fig. 7b), which is notably lower than those of NF/Ni_3S_2/MnS (136 mV), NF/MnO_2 (195 mV), and so far reported MnO_x and other metal oxides/sulfides (Fig. 7e, Table S1) [8,29,42–47]. NF has no obvious electrocatalytic activity for HER and following OER, simply acting as current collector, as shown in Fig. S7a and b. Meanwhile, the Tafel slope for NF/T(Ni_3S_2/MnS-O) is calculated to be 41 mV dec^{-1} (Fig. 7c), close to that of commercial Pt/C (36 mV dec^{-1}), and much lower than those of reported metal oxides and sulfides (Fig. 7e, Table S1), suggesting a fast HER kinetics *via* a Volmer–Heyrovsky routes [48]. OVs

adjacent to M (M = Mn or Ni atom) sites decrease the free energy in the adsorption process of H_{ads} on M to form M-H_{ads} ($H_2O + M + e^- \rightarrow$ M-$H_{ads} + OH^-$, Step 1, Volmer step, Fig. 7a), as well as the desorption of H_2 (M-$H_{ads} + H_2O + e^- \rightarrow M + H_2 + OH^-$, Steps 2–3, Heyrovsky step) [48,49]. So together with hierarchical pores ensuring sufficient exposure of OVs, the HER kinetics greatly speeds up. These results indicate a much more rapid speed when using NF/T(Ni_3S_2/MnS-O) as the HER electrocatalyst. According to electrochemical impedance spectroscopy (EIS), the Nyquist plots (Fig. 7d) reveal that the charge transfer resistance (R_{ct}) value of the NF/T(Ni_3S_2/MnS-O) (0.37 Ω) is obviously smaller than those of NF/Ni_3S_2/MnS (0.69 Ω) and NF/MnO_2 (0.93 Ω), suggesting the rapid charge-transfer.

The excellent stability of NF/T(Ni_3S_2/MnS-O) is further confirmed by a chronopotentiometry test with a nearly unchanged operating overpotential after 50 h at a cathode current of $-10 mA cm^{-2}$ (Fig. 7f). The NF/TU(Ni_3S_2/MnS-O) shows no obvious changes in morphology and EDS peaks, as well as no new diffraction peak appearing in XRD pattern after 50 h of HER (Fig. S8), indicating that NF/TU(Ni_3S_2/MnS-O) is not reduced to NF/Ni_3S_2/MnS The amount of H_2 gas generated in 60 min at a voltage of -0.50 V (*vs.* RHE) is 589 μmol (Fig. 7g), which is in good agreement with the theoretically calculated value (575 μmol), indicating the faradaic efficiency of NF/T(Ni_3S_2/MnS-O) for the HER is nearly 100%. The result also demonstrates that the transferred electrons are completely used for HER and not used for reducing NF/T(Ni_3S_2/MnS-O) as metallic or sulfide nanoparticles.

In addition to excellent HER performance, OER performance of NF/T(Ni_3S_2/MnS-O) is also examined to be excellent (Movie S2). OVs also feature low coordination, so in the OER process, together with hierarchical pores ensuring sufficient exposure of OVs [50], the adsorption of OH^- is favorable for forming $M - OH_{ads}$ (Fig. 8a, Step 1) [23]. In the subsequent rate-determining step [50,51], OVs lower down the free energy of the conversion of $M - OH_{ads}$ to form active intermediates (M-O_{ads}, $M - OOH_{ads}$, Steps 2–3), thereby speeding up the OER kinetics. The overpotential at a current density of 10 $mA cm^{-2}$ of NF/T(Ni_3S_2/MnS-O) reaches 228 mV (Fig. 8b), lower than those of NF/Ni_3S_2/MnS (279 mV), NF/MnO_2 (283 mV), commercial IrO_2 (298 mV) and so far reported MnO_x [8,52] and other metal oxides [29,46,53] /sulfides [33,54–56] (Fig. 8e, Tables S1–S2), indicating that NF/T(Ni_3S_2/MnS-O) has a better OER catalytic activity. The Tafel slope value of NF/T(Ni_3S_2/MnS-O) is 46 mV dec^{-1} (Fig. 8c), much lower than those of NF/Ni_3S_2/MnS (53 mV dec^{-1}), NF/MnO_2 (60 mV dec^{-1}), commercial IrO_2 (52 mV dec^{-1}) and so far the lowest values among reported metal oxides/sulfides (Fig. 8e, Tables S1–S2), indicating the fastest OER. The
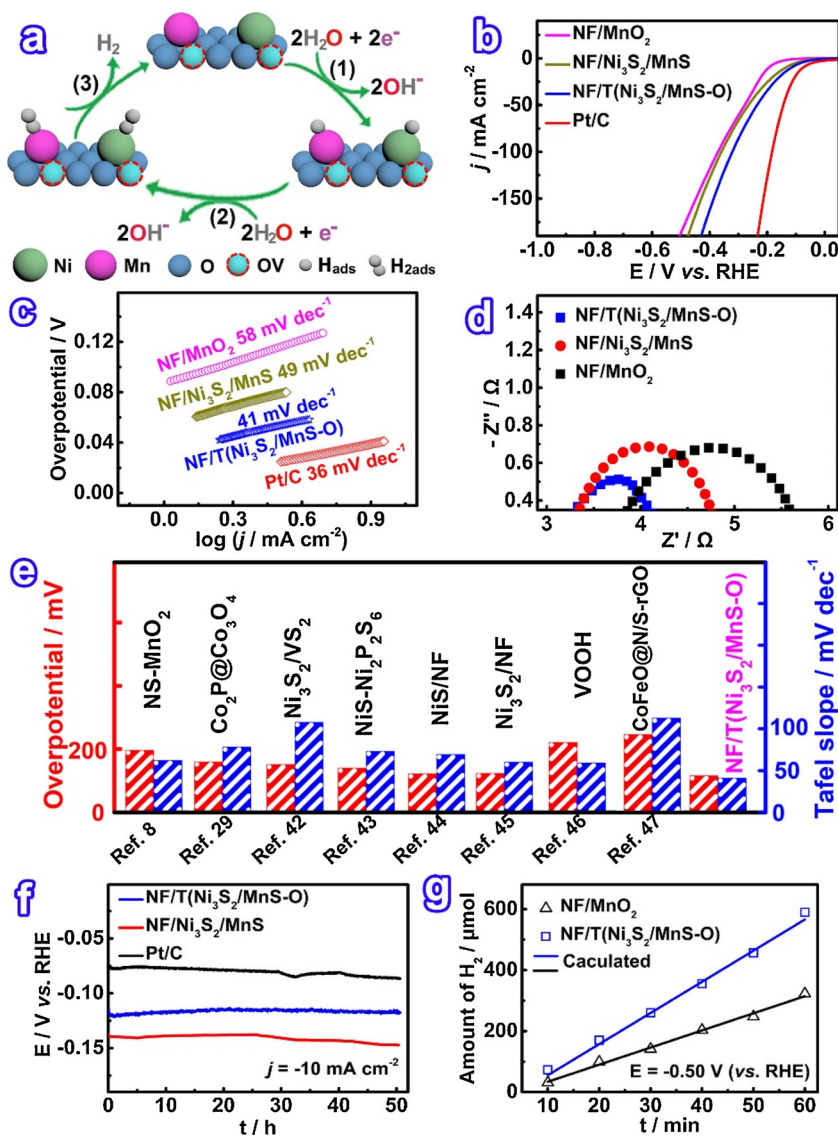
Fig. 7. (a) Schematics of the HER pathways with Mn and Ni atoms adjacent to OV as active sites. Only one OV near Mn or Ni atom is illustrated. (b) Linear sweep voltammetry (LSV) curves of NF/T(Ni_3S_2/MnS-O), NF/Ni_3S_2/MnS, NF/MnO_2, and the commercial Pt/C in 1.0 M KOH at a scan rate of 5 mV s^{-1} and (c) corresponding Tafel plots. (d) Nyquist plots of NF/MnO_2, NF/Ni_3S_2/MnS and NF/T(Ni_3S_2/MnS-O) at the overpotential of 300 mV for HER. (e) Comparison of overpotential and Tafel slope of HER for the NF/T(Ni_3S_2/MnS-O) and reported metal oxides and sulfides [8,29,42–47]. (f) Long-term stability under a constant current density of 10 mA cm^{-2} of NF/T(Ni_3S_2/MnS-O), NF/Ni_3S_2/MnS and Pt/C. (g) H_2 amount evolved from the NF/T(Ni_3S_2/MnS-O) and NF/MnO_2 electrodes over time at a voltage of −0.50 V (*vs.* RHE).

EIS results reveal that the R_{ct} for NF/T(Ni_3S_2/MnS-O) (0.71 Ω) is smaller than those of NF/Ni_3S_2/MnS (0.97 Ω) and NF/MnO_2 (1.06 Ω) (Fig. 8d), demonstrating a rapid charge-transfer process.

Only slight potential changes at a current density of 10 mA cm^{-2} for 50 h (Fig. 8f), indicating the good long-term OER activity for the NF/T(Ni_3S_2/MnS-O). The XRD peaks of NF/Ni_3S_2/MnS before and after 50 h of OER have no obvious changes and do not shift to higher angles (Fig. S9), compared with that of NF/T(Ni_3S_2/MnS-O) (Fig. 4), indicating NF/Ni_3S_2/MnS are not oxidized to reconstruct into the desired NF/T(Ni_3S_2/MnS-O) in OER process. The NF/T(Ni_3S_2/MnS-O) should be formed during electrooxidation of the NF/Ni_3S_2/MnS under a relatively high potential (1.6 V *vs.* RHE). After 50 h of OER, no changes occur in SEM image of NF/T(Ni_3S_2/MnS-O) (Fig. S10), although there are some new peaks occurring in XRD, corresponding to MnOOH and NiOOH, respectively, indicating the Ni_3S_2 and MnS are both oxidized. In addition, there are no obvious changes in XPS spectra and corresponding element contents, indicating the surface chemistry of NF/T(Ni_3S_2/MnS-O) is not changed (Fig. S11). The reason of the decline of voltage appearing at 25 h may be due to slightly accumulated gaseous O_2 on surface of electrode. The amount of generated O_2 gas is measured at a voltage of 1.65 V (*vs.* RHE) (Fig. 8g). The amount of experimentally generated O_2 (191 μmol) in 60 min matches very well with theoretically calculated value (198 μmol), indicating a faradaic efficiency of nearly

100% [47]. Moreover, the turnover frequency (0.25 s^{-1} site^{-1}) of NF/T(Ni_3S_2/MnS-O) at the overpotential of 300 mV is larger than NF/Ni_3S_2/MnS (0.04 s^{-1} site^{-1}), NF/MnO_2 (0.03 s^{-1} site^{-1}) and other reported catalysts (Fig. S12, Table S3), suggesting NF/T(Ni_3S_2/MnS-O) exhibits the excellent surface electronic structure of NF/T(Ni_3S_2/MnS-O) that facilitate electron and mass transfer process [57].

Compared with NF/Ni_3S_2 (Fig. S7c and d), NF/Ni_3S_2/MnS shows smaller overpotentials for both HER (Fig. 7b) and OER (Fig. 8b), indicating NF/Ni_3S_2/MnS shows better electrocatalytic activity. The results also demonstrate that the heterostructure can optimize the interface electron structure to an enhanced intrinsic catalytic activity, as also reported for CoS_x/Ni_3S_2 nanosheets [54] and Co–Ni–S–P microspheres [58]. However, the performances of NF/Ni_3S_2 and NF/Ni_3S_2/MnS are still not as good as that of NF/T(Ni_3S_2/MnS-O), indicating that the metal oxides layer with abundant OVs is beneficial to improve electrocatalytic performance.

Based on the excellent electrocatalytic activity and stability of NF/T(Ni_3S_2/MnS-O) for both HER and OER in alkaline media, a two-electrode electrolyzer is assembled by using NF/T(Ni_3S_2/MnS-O) directly as cathode and anode, respectively, in 1.0 M KOH for the overall water splitting (Fig. 9a). The NF/T(Ni_3S_2/MnS-O) achieves a voltage of only 1.54 V, with an overpotential of 0.31 V at a current density of 10 mA cm^{-2} (Fig. 9b), lower than those of Pt/C//IrO_2 (1.56 V, 0.33 V)
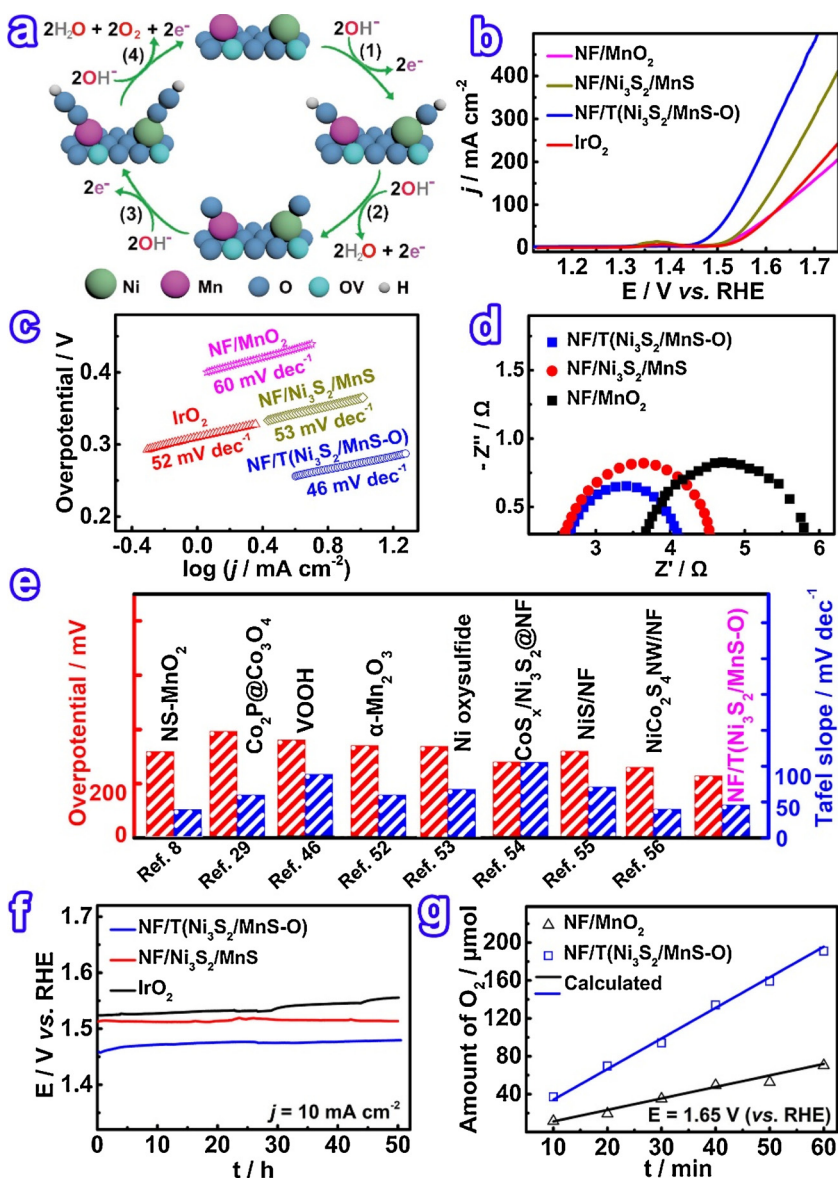
Fig. 8. (a) Schematics of the OER pathways with Mn and Ni atoms adjacent to OV as active sites. Only one OV near Mn or Ni atom is illustrated. (b) LSV curves of NF/T(Ni$_3$S$_2$/MnS-O), NF/Ni$_3$S$_2$/MnS, NF/MnO$_2$, and commercial IrO$_2$ in 1.0 M KOH at a scan rate of 5 mV s^{-1} and (c) corresponding Tafel plots. (d) Nyquist plots of NF/MnO$_2$, NF/Ni$_3$S$_2$/MnS and NF/T(Ni$_3$S$_2$/MnS-O) at the overpotential of 300 mV for OER. (e) Comparison of overpotential and Tafel slope of OER between the NF/T(Ni$_3$S$_2$/MnS-O) and reported metal oxides and sulfides [8,29,46,52–56]. (f) Long-term stability under a constant current density of 10 mA cm^{-2} of NF/T(Ni$_3$S$_2$/MnS-O), NF/Ni$_3$S$_2$/MnS and IrO$_2$. (g) O$_2$ amount evolved from the NF/T(Ni$_3$S$_2$/MnS-O) and NF/MnO$_2$ electrodes over time at a voltage of 1.65 V (*vs.* RHE).

and reported metal oxides (MnO$_x$ not reported yet) [29,46,47,59] /sulfides [43,44,53–57,60–62] (Fig. 9c, Table S1). The R_{ct} of the NF/T(Ni$_3$S$_2$/MnS-O) is 2.14 Ω, smaller than those of NF/Ni$_3$S$_2$/MnS (2.87 Ω) and NF/MnO$_2$ (3.86 Ω) (Fig. S13), implying better access of electrolyte to the electrocatalyst surface and a faster charge transfer on surface of the NF/T(Ni$_3$S$_2$/MnS-O). Importantly, the NF/T(Ni$_3$S$_2$/MnS-O)//NF/T(Ni$_3$S$_2$/MnS-O) displays outstanding stability with negligible potential change at 10 mA cm^{-2} for 50 h (Fig. 9d). The morphologies of NF/T(Ni$_3$S$_2$/MnS-O) as cathode and anode, respectively, are not obviously changed after 50 h of water splitting (Fig. S14), indicating the structural stability of NF/T(Ni$_3$S$_2$/MnS-O). In addition, the abundant gas evolution from both electrodes could be clearly observed during overall water splitting (Movie S3). The gas yield for both O$_2$ and H$_2$ at the applied potential of 1.6 V shows a good linear relationship with the splitting time (Fig. 9e). The experimentally measured gas evolution speed is 4.13 and 2.04 μmol min^{-1} for H$_2$ and O$_2$, respectively, both faster than those of reported electrocatalysts (Table S4). The slope ratio of 2.02 is close to the theoretical ratio of 2, indicating the faradaic efficiency for water splitting is nearly 100% and the transferred electrons are completely used for water splitting.

4. Conclusion

In summary, tremella-like Ni$_3$S$_2$/MnS with ultrathin nanosheets, abundant OVs and hierarchical pores is grown on NF. The OVs improve conductivity, facilitate the kinetic processes of the adsorption of H$_2$O for HER or OH$^-$ for OER, the evolution and desorption of H$_2$ or O$_2$. Moreover, hierarchical porous structure and high active surface area assure sufficient exposure of OVs and facilitate the mass transfer of H$_2$O for HER or OH$^-$ for OER to and H$_2$ or O$_2$ from NF/T(Ni$_3$S$_2$/MnS-O), synergistically speeding up HER or OER, and yielding better bifunctional HER or OER performances than so far reported MnO$_x$ and other metal oxides/sulfides. Consequently, the NF/T(Ni$_3$S$_2$/MnS-O) exhibits excellent HER and OER bifunctional performance for overall water splitting when used directly as electrodes, including lower cell voltage, faster H$_2$ and O$_2$ evolution speed than those of so far reported metal oxides (MnO$_x$ not reported yet) /sulfides. This work provides a new path to obtain highly efficient non-noble metal electrocatalysts by inducing OVs to Ni$_3$S$_2$/MnS through electrooxidation for meeting demands of green energy.
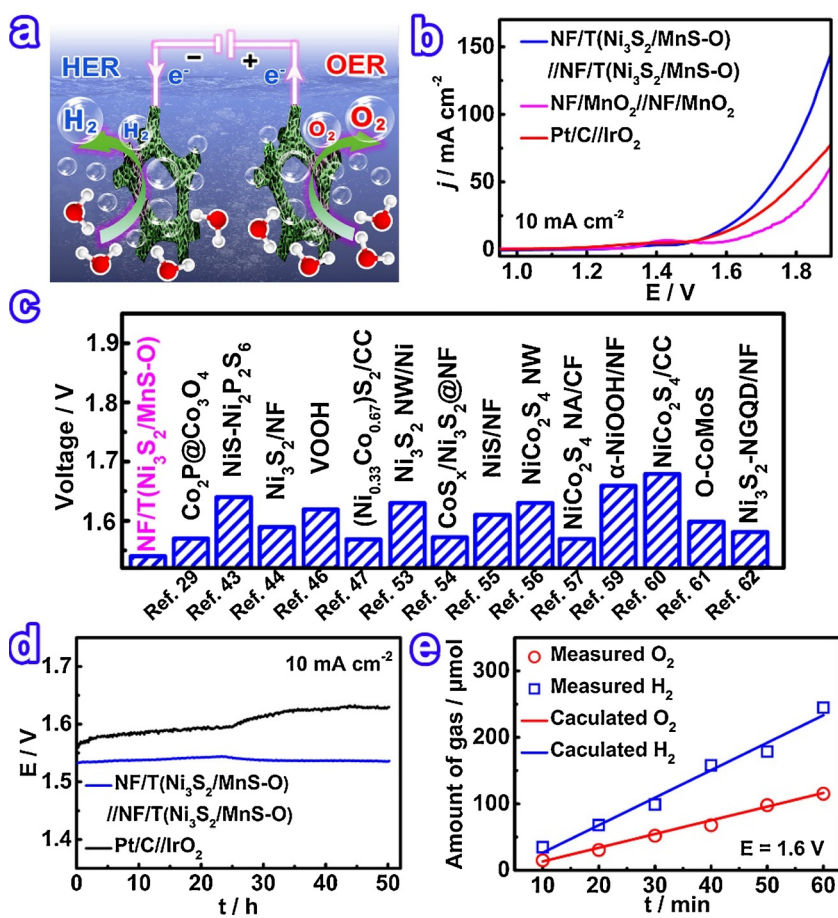
Fig. 9. (a) Schematic of electrocatalyzing overall water splitting on NF/T(Ni$_3$S$_2$/MnS-O). (b) LSV curves of water electrolysis in a two-electrode system. (c) Comparison of water splitting voltage at the current density of 10 mA cm^{-2} for NF/T(Ni$_3$S$_2$/MnS-O) and reported metal oxides and sulfides [29,43,44,46,47,53–57,59–62]. (d) Chronopotentiometry responses of NF/T(Ni$_3$S$_2$/MnS-O)//NF/T(Ni$_3$S$_2$/MnS-O) and Pt/C//IrO$_2$ at a constant current density of 10 mA cm^{-2} in 1.0 M KOH. (e) Amount of O$_2$ and H$_2$ evolved from the NF/T(Ni$_3$S$_2$/MnS-O) electrode over time at a voltage of 1.6 V.

Acknowledgements

Appendix A. Supplementary data

Supplementary material related to this article can be found, in the online version, at doi:https://doi.org/10.1016/j.apcatb.2019.117899.

References

[1] C.Q. Dong, T.Y. Kou, H. Gao, Z.Q. Peng, Z.H. Zhang, Eutectic-derived mesoporous Ni-Fe-O nanowire network catalyzing oxygen evolution and overall water splitting, Adv. Energy Mater. 8 (2018) 1701347, , https://doi.org/10.1002/aenm.201701347.

[2] Z.W. Seh, J. Kibsgaard, C.F. Dickens, I.B. Chorkendorff, J.K. Norskov, T.F. Jaramillo, Combining theory and experiment in electrocatalysis: Insights into materials design, Science 355 (2017) eaad4998, , https://doi.org/10.1126/science.aad4998.

[3] C. Wei, Z.J. Xu, The comprehensive understanding of as an evaluation parameter for electrochemical water splitting, Small Methods 2 (2018) 1800168, , https://doi.org/10.1002/smtd.201800168.

[4] C.C.L. McCrory, S. Jung, I.M. Ferrer, S.M. Chatman, J.C. Peters, T.F. Jaramillo, Benchmarking hydrogen evolving reaction and oxygen evolving reaction electrocatalysts for solar water splitting devices, J. Am. Chem. Soc. 137 (2015) 4347–4357, https://doi.org/10.1021/ja510442p.

[5] I. Roger, M.A. Shipman, M.D. Symes, Earth-abundant catalysts for electrochemical and photoelectrochemical water splitting, Int. Rev. Chem. Eng. 1 (2017) 0003, https://doi.org/10.1038/s41570-016-0003.

[6] Y.F. Yu, Y.M. Shi, B. Zhang, Synergetic transformation of solid inorganic–organic hybrids into advanced nanomaterials for catalytic water splitting, Acc. Chem. Res. 51 (2018) 1711–1721, https://doi.org/10.1021/acs.accounts.8b00193.

[7] J. Li, G.F. Zheng, One-dimensional earth-abundant nanomaterials for water-splitting electrocatalysts, Adv. Sci. 4 (2017) 1600380, , https://doi.org/10.1002/advs.201600380.

[8] Y.X. Zhao, C. Chang, F. Teng, Y.F. Zhao, G.B. Chen, R. Shi, G.I.N. Waterhouse, W.F. Huang, T.R. Zhang, Defect-engineered ultrathin δ-MNO$_2$ nanosheet arrays as bifunctional electrodes for efficient overall water splitting, Adv. Energy Mater. 7 (2017) 1700005, , https://doi.org/10.1002/aenm.201700005.

[9] Y.J. Wang, H. Wu, L. Huang, H. Zhao, Z.F. Liu, X.C. Chen, H. Liu, Y. Zhang, Hierarchically porous N,S-codoped carbon-embedded dual phase MnO/MnS nanoparticles for efficient lithium ion storage, Inorg. Chem. 57 (2018) 7993–8001, https://doi.org/10.1021/acs.inorgchem.8b01156.

[10] P.B. Geng, S.S. Zheng, H. Tang, R.M. Zhu, L. Zhang, S. Cao, H.G. Xue, H. Pang, Transition metal sulfides based on graphene for electrochemical energy storage, Adv. Energy Mater. 8 (2018) 1703259, , https://doi.org/10.1002/aenm.201703259.

[11] Z. Zhang, S. Liu, F. Xiao, S. Wang, Facile synthesis of heterostructured nickel/nickel oxide wrapped carbon fiber: Flexible bifunctional gas-evolving electrode for highly efficient overall water splitting, ACS Sustain. Chem. Eng. 5 (2017) 529–536, https://doi.org/10.1021/acssuschemeng.6b01879.

[12] L. Ma, H. Fan, K. Fu, S. Lei, Q. Hu, H. Huang, G. He, Protonation of graphitic carbon nitride (g-C$_3$N$_4$) for an electrostatically self-assembling carbon@g-C$_3$N$_4$core-shell nanostructure toward high hydrogen evolution, ACS Sustain. Chem. Eng. 5 (2017) 7093–7103, https://doi.org/10.1021/acssuschemeng.7b01312.

[13] C. Wang, H. Fan, X. Ren, Y. Wen, W. Wang, Highly Dispersed PtO nanodots as efficient co-catalyst for photocatalytic hydrogen evolution, Appl. Surf. Sci. 462 (2018) 423–431, https://doi.org/10.1016/j.apsusc.2018.08.126.

[14] H. Tian, H. Fan, J. Ma, L. Ma, G. Dong, Noble metal-free modified electrode of exfoliated graphitic carbon nitride/ZnO nanosheets for highly efficient hydrogen peroxide sensing, Electrochim. Acta 247 (2017) 787–794, https://doi.org/10.1016/j.electacta.2017.07.083.

[15] M. Zhang, H. Fan, X. Ren, N. Zhao, H. Peng, C. Wang, X. Wu, G. Dong, C. Long, W. Wang, Y. Gao, L. Ma, P. Wu, H. Li, X. Jiang, Study of pseudocapacitive contribution to superior energy storage of 3D heterostructure CoWO$_4$/Co$_3$O$_4$ nanocone arrays, J. Power Sources 418 (2019) 202–210, https://doi.org/10.1016/j.jpowsour.2019.02.041.

[16] A. Wu, Y. Xie, H. Ma, C. Tian, Y. Gu, H. Yan, X. Zhang, G. Yang, H. Fu, Integrating the active OER and HER components as the heterostructures for the efficient overall water splitting, Nano Energy 44 (2018) 353–363, https://doi.org/10.1016/j.nanoen.2017.11.045.

[17] S. Jin, Are metal chalcogenides, nitrides, and phosphides oxygen evolution catalysts or bifunctional catalysts? ACS Energy Lett. 2 (2017) 1937–1938, https://doi.org/

10.1021/acsenergylett.7b00679.

[18] J. Yin, Y.X. Li, F. Lv, M. Lu, K. Sun, W. Wang, L. Wang, F.Y. Cheng, Y.F. Li, P.X. Xi, S.J. Guo, Oxygen vacancies dominated NiS$_2$/CoS$_2$ interface porous nanowires for portable Zn-Air batteries driven water splitting devices, Adv. Mater. 29 (2017) 1704681, , https://doi.org/10.1002/adma.201704681.

[19] L. Li, X.H. Feng, Y. Nie, S.G. Chen, F. Shi, K. Xiong, W. Ding, X.Q. Qi, J.S. Hu, Z.D. Wei, L.J. Wan, M.R. Xia, Insight into the effect of oxygen vacancy concentration on the catalytic performance of MnO$_2$, ACS Catal. 5 (2015) 4825–4832, https://doi.org/10.1021/acscatal.5b00320.

[20] F.Y. Cheng, T.R. Zhang, Y. Zhang, J. Du, X.P. Han, J. Chen, Enhancing electrocatalytic oxygen reduction on MnO$_2$ with vacancies, Angew. Chem. Int. Ed. 52 (2013) 2474–2477, https://doi.org/10.1002/anie.201208582.

[21] Y. Zheng, Y. Jiao, M. Jaroniec, S.Z. Qiao, Advancing the electrochemistry of the hydrogen-evolution reaction through combining experiment and theory, Angew. Chem. Int. Ed. 54 (2015) 52–65, https://doi.org/10.1002/anie.201407031.

[22] J. Kim, P. Shih, Y. Qin, Z. Al-Bardan, C.J. Sun, H. Yang, A porous pyrochlore Y$_2$[Ru$_{1.6}$Y$_{0.4}$]O$_{7-\delta}$ electrocatalyst for enhanced performance towards the oxygen evolution reaction in acidic media, Angew. Chem. Int. Ed. 57 (2018) 13877–13881, https://doi.org/10.1002/anie.201808825.

[23] M.Q. Yang, J. Wang, H. Wu, G.W. Ho, Noble metal-free nanocatalysts with vacancies for electrochemical water splitting, Small 14 (2018) 1703323, , https://doi.org/10.1002/smll.201703323.

[24] N.N. Han, K.R. Yang, Z.Y. Lu, Y.J. Li, W.W. Xu, T.F. Gao, Z. Cai, Y. Zhang, V.S. Batista, W. Liu, X.M. Sun, Nitrogen-doped tungsten carbide nanoarray as an efficient bifunctional electrocatalyst for water splitting in acid, Nat. Commun. 9 (2018) 924, https://doi.org/10.1038/s41467-018-03429-z.

[25] W. Chen, H. Wang, Y. Li, Y. Liu, J. Sun, S. Lee, J.S. Lee, Y. Cui, In situ electrochemical oxidation tuning of transition metal disulfides to oxides for enhanced water oxidation, ACS Cent. Sci. 1 (2015) 244–251, https://doi.org/10.1021/acscentsci.5b00227.

[26] W.W. Xu, Z.Y. Lu, X.M. Sun, L. Jiang, X. Duan, Superwetting electrodes for gas-involving electrocatalysis, Acc. Chem. Res. 51 (2018) 1590–1598, https://doi.org/10.1021/acs.accounts.8b00070.

[27] K. Mette, A. Bergmann, J.P. Tessonnier, M. Haevecker, L.D. Yao, T. Ressler, R. Schloegl, P. Strasser, M. Behrens, Nanostructured manganese oxide supported on carbon nanotubes for electrocatalytic water splitting, Chem. Cat. Chem. 4 (2012) 851–862, https://doi.org/10.1002/cctc.201100434.

[28] G.Q. Zhang, Y.F. Li, Yf. Zhou, F.L. Yang, NiFe layered-double-hydroxide-derived NiO-NiFe$_2$O$_4$/reduced graphene oxide architectures for enhanced electrocatalysis of alkaline water splitting, ChemElectroChem 3 (2016) 1927–1936, https://doi.org/10.1002/celc.201600301.

[29] L.H. Yao, N. Zhang, Y. Wang, Y.M. Ni, D.P. Yan, C.W. Hu, Facile formation of 2D Co$_2$P@Co$_3$O$_4$ microsheets through in-situ toptactic conversion and surface corrosion: bifunctional electrocatalysts towards overall water splitting, J. Power Sources 374 (2018) 142–148, https://doi.org/10.1016/j.jpowsour.2017.11.028.

[30] F. Qin, Z.H. Zhao, M.K. Alam, Y.Z. Ni, F. Robles-Hernandez, L. Yu, S. Chen, Z.F. Ren, Z.M. Wang, J.M. Bao, Trimetallic NiFeMo for overall electrochemical water splitting with a low cell voltage, ACS Energy Lett. 3 (2018) 546–554, https://doi.org/10.1021/acsenergylett.7b01335.

[31] J. Kibsgaard, Z. Chen, B.N. Reinecke, T.F. Jaramillo, Engineering the surface structure of MoS2 to preferentially expose active edge sites for electrocatalysis, Nat. Mater. 11 (2012) 963, https://doi.org/10.1038/nmat3439.

[32] G. Zhang, Y.S. Feng, W.T. Lu, D. He, C.Y. Wang, Y.K. Li, X.Y. Wang, F.F. Cao, Enhanced catalysis of electrochemical overall water splitting in alkaline media by Fe doping in Ni$_3$S$_2$ nanosheet arrays, ACS Catal. 8 (2018) 5431–5441, https://doi.org/10.1021/acscatal.8b00413.

[33] A. Sivanantham, P. Ganesan, S. Shanmugam, Hierarchical NiCo$_2$S$_4$ nanowire arrays supported on Ni foam: An efficient and durable bifunctional electrocatalyst for oxygen and hydrogen evolution reactions, Adv. Funct. Mater. 26 (2016) 4661–4672, https://doi.org/10.1002/adfm.201600566.

[34] J.G. Zhang, Y. Li, T.Y. Zhu, Y. Wang, J.W. Cui, J.J. Wu, H. Xu, X. Shu, Y.Q. Qin, H.M. Zheng, P.M. Ajayan, Y. Zhang, Y.C. Wu, 3D coral-like Ni$_3$S$_2$ on Ni foam as a bifunctional electrocatalyst for overall water splitting, ACS Appl. Mater. Interfaces 10 (2018) 31330–31339, https://doi.org/10.1021/acsami.8b09361.

[35] Y. Liu, L. Li, J. Zhu, T. Meng, L. Ma, H. Zhang, M. Xu, J. Jiang, C.M. Li, One-dimensional integrated MnS@carbon nanoreactors hybrid: an Alternative anode for full-cell Li-ion and Na-ion batteries, ACS Appl. Mater. Interfaces 10 (2018) 27911–27919, https://doi.org/10.1021/acsami.8b05688.

[36] S.C. Wang, P. Chen, Y. Bai, J.H. Yun, G. Liu, L.Z. Wang, New BiVO$_4$ dual photoanodes with enriched oxygen vacancies for efficient solar-driven water splitting, Adv. Mater. 30 (2018) 1800486, , https://doi.org/10.1002/adma.201800486.

[37] X. Zheng, Y. Zhang, H. Liu, D. Fu, J. Chen, J. Wang, C. Zhong, Y. Deng, X. Han, W. Hu, In situ fabrication of heterostructure on nickel foam with tuned composition for enhancing water-splitting performance, Small 14 (2018) 1803666, , https://doi.org/10.1002/smll.201803666.

[38] J. Diao, W. Yuan, Y. Qiu, L. Cheng, X. Guo, A hierarchical oxygen vacancy-rich WO$_3$ with "nanowire-array-on-nanosheet-array" structure for highly efficient oxygen evolution reaction, J. Mater. Chem. A 7 (2019) 6730–6739, https://doi.org/10.1039/C9TA01044K.

[39] H. Tian, H. Fan, J. Ma, Z. Liu, L. Ma, S. Lei, J. Fang, C. Long, Pt-decorated zinc oxide nanorod arrays with graphitic carbon nitride nanosheets for highly efficient dual-functional gas sensing, J. Hazard. Mater. 341 (2018) 102–111, https://doi.org/10.1016/j.jhazmat.2017.07.056.

[40] X. Shang, B. Dong, Y.M. Chai, C.G. Liu, In-situ electrochemical activation designed hybrid electrocatalysts for water electrolysis, Sci. Bull. 63 (2018) 853–876, https://doi.org/10.1016/j.scib.2018.05.014.

[41] A.J. Nelson, J.G. Reynolds, J.W. Roos, Core-level satellites and outer core-level multiplet splitting in Mn model compounds, J. Vac. Sci. Technol. A 18 (2000) 1072–1076, https://doi.org/10.1116/1.582302.

[42] X.W. Zhong, J. Tang, J.W. Wang, M.M. Shao, J.W. Chai, S.P. Wang, M. Yang, Y. Yang, N. Wang, S.J. Wang, B.M. Xu, H. Pan, 3D heterostructured pure and N-doped Ni$_3$S$_2$/VS$_2$ nanosheets for high efficient overall water splitting, Electrochim. Acta 269 (2018) 55–61, https://doi.org/10.1016/j.electacta.2018.02.131.

[43] X.Y. Zhang, S. Zhang, J. Li, E.K. Wang, One-step synthesis of well-structured NiS-Ni$_2$P$_2$S$_6$ nanosheets on nickel foam for efficient overall water splitting, J. Mater. Chem. A 5 (2017) 22131–22136, https://doi.org/10.1039/c7ta05285e.

[44] H.N. Ren, Z.H. Huang, Z.Y. Yang, S.J. Tang, F.Y. Kang, R.T. Lv, Facile synthesis of free-standing nickel chalcogenide electrodes for overall water splitting, J. Energy Chem. 26 (2017) 1217–1222, https://doi.org/10.1016/j.jechem.2017.10.004.

[45] W.X. Zhu, X.Y. Yue, W.T. Zhang, S.X. Yu, Y.H. Zhang, J. Wang, J.L. Wang, Nickel sulfide microsphere film on Ni foam as an efficient bifunctional electrocatalyst for overall water splitting, Chem. Commun. (Camb.) 52 (2016) 1486–1489, https://doi.org/10.1039/c5cc08064a.

[46] H.H. Shi, H.F. Liang, F.W. Ming, Z.C. Wang, Efficient overall water-splitting electrocatalysis using lepidocrocite VOOH hollow nanospheres, Angew. Chem. Int. Ed. 56 (2017) 573–577, https://doi.org/10.1002/anie.201610211.

[47] B.H. Zhang, H.X. Wang, Z. Zuo, H.S. Wang, J.T. Zhang, Tunable CoFe-based active sites on 3D heteroatom doped graphene aerogel electrocatalysts via annealing gas regulation for efficient water splitting, J. Mater. Chem. A 6 (2018) 15728–15737, https://doi.org/10.1039/C8TA05705B.

[48] Z. Luo, R. Miao, T.D. Huan, I.M. Mosa, A.S. Poyraz, W. Zhong, J.E. Cloud, D.A. Kriz, S. Thanneeru, J.K. He, Y.S. Zhang, R. Ramprasad, S.L. Suib, Mesoporous MoO$_{3-x}$ material as an efficient electrocatalyst for hydrogen evolution reactions, Adv. Energy Mater. 6 (2016) 1600528, , https://doi.org/10.1002/aenm.201600528.

[49] T. Zhang, M.Y. Wu, D.Y. Yan, J. Mao, H. Liu, W.B. Hu, X.W. Du, T. Ling, S.Z. Qiao, Engineering oxygen vacancy on NiO nanorod arrays for alkaline hydrogen evolution, Nano Energy 43 (2018) 103–109, https://doi.org/10.1016/j.nanoen.2017.11.015.

[50] C.L. Hu, L. Zhang, Z.J. Zhao, J. Luo, J. Shi, Z.Q. Huang, J.L. Gong, Edge sites with unsaturated coordination on core–shell Mn$_3$O$_4$@Mn$_x$Co$_{3-x}$O$_4$ nanostructures for electrocatalytic water oxidation, Adv. Mater. 29 (2017) 1701820, , https://doi.org/10.1002/adma.201701820.

[51] J. Sun, N.K. Guo, Z.Y. Shao, K.K. Huang, Y.W. Li, F. He, Q. Wang, A facile strategy to construct amorphous spinel-based electrocatalysts with massive oxygen vacancies using ionic liquid dopant, Adv. Energy Mater. 8 (2018) 1800980, , https://doi.org/10.1002/aenm.201800980.

[52] M. Kölbach, S. Fiechter, R. van de Krol, P. Bogdanoff, Evaluation of electrodeposited α-Mn$_2$O$_3$ as a catalyst for the oxygen evolution reaction, Catal. Today 290 (2017) 2–9, https://doi.org/10.1016/j.cattod.2017.03.030.

[53] J.L. Liu, Y. Yang, B. Ni, H.Y. Li, X. Wang, Fullerene-like nickel oxysulfide hollow nanospheres as bifunctional electrocatalysts for water splitting, Small 13 (2017) 1602637, , https://doi.org/10.1002/smll.201602637.

[54] S. Shit, S. Chhetri, W. Jang, N.C. Murmu, H. Koo, P. Samanta, T. Kuila, Cobalt sulfide/nickel sulfide heterostructure directly grown on nickel foam: an efficient and durable electrocatalyst for overall water splitting application, ACS Appl. Mater. Interfaces 10 (2018) 27712–27722, https://doi.org/10.1021/acsami.8b04223.

[55] J.T. Ren, Z.Y. Yuan, Hierarchical nickel sulfide nanosheets directly grown on Ni foam: a stable and efficient electrocatalyst for water reduction and oxidation in alkaline medium, ACS Sustainable Chem. Eng. 5 (2017) 7203–7210, https://doi.org/10.1021/acssuschemeng.7b01419.

[56] D.N. Liu, Q. Lu, Y.L. Luo, X.P. Sun, A.M. Asiri, NiCo$_2$S$_4$ nanowires array as an efficient bifunctional electrocatalyst for full water splitting with superior activity, Nanoscale 7 (2015) 15122–15126, https://doi.org/10.1039/c5nr04064g.

[57] Y. Wang, J. Ma, J. Wang, S. Chen, H. Wang, J. Zhang, Interfacial scaffolding preparation of hierarchical PBA-based derivative electrocatalysts for efficient water splitting, Adv. Energy Mater. 9 (2019) 1802939, , https://doi.org/10.1002/aenm.201802939.

[58] H.J. Song, H. Yoon, B. Ju, G.-H. Lee, D.-W. Kim, 3D architectures of quaternary Co-Ni-S-P/graphene hybrids as highly active and stable bifunctional electrocatalysts for overall water splitting, Adv. Energy Mater. 8 (2018) 1802319, , https://doi.org/10.1002/aenm.201802319.

[59] Q. Zhang, C.C. Zhang, J.B. Liang, P.G. Yin, Y. Tian, Orthorhombic α-NiOOH nanosheet arrays: phase conversion and efficient bifunctional electrocatalysts for full water splitting, ACS Sustainable Chem. Eng. 5 (2017) 3808–3818, https://doi.org/10.1021/acssuschemeng.6b02788.

[60] Q. Zhang, C. Ye, X.L. Li, Y.H. Deng, B.X. Tao, W. Xiao, L.J. Li, N.B. Li, H.Q. Luo, Self-interconnected porous networks of NiCo disulfide as efficient bifunctional electrocatalysts for overall water splitting, ACS Appl. Mater. Interfaces 10 (2018) 27723–27733, https://doi.org/10.1021/acsami.8b04386.

[61] J.G. Hou, B. Zhang, Z.W. Li, S.Y. Cao, Y.Q. Sun, Y.Z. Wu, Z.M. Gao, L.C. Sun, Vertically aligned oxygenated-CoS$_2$-MoS$_2$ heteronanosheet architecture from polyoxometalate for efficient and stable overall water splitting, ACS Catal. 8 (2018) 4612–4621, https://doi.org/10.1021/acscatal.8b00668.

[62] J.J. Lv, J. Zhao, H. Fang, L.P. Jiang, L.L. Li, J. Ma, J.J. Zhu, Incorporating nitrogen-doped graphene quantum dots and Ni$_3$S$_2$ nanosheets: a synergistic electrocatalyst with highly enhanced activity for overall water splitting, Small 13 (2017) 1700264, , https://doi.org/10.1002/smll.201700264.